



Original Article

Quantification of Trace-Level Silicon Doping in $\text{Al}_x\text{Ga}_{1-x}\text{N}$ Films Using Wavelength-Dispersive X-Ray Microanalysis

Lucia Spasevski^{1*} , Ben Buse², Paul R. Edwards¹ , Daniel A. Hunter¹, Johannes Enslin³, Humberto M. Foronda³, Tim Wernicke³, Frank Mehnke³, Peter J. Parbrook⁴, Michael Kneissl^{3,5} and Robert W. Martin^{1*}

¹Department of Physics, SUPA, University of Strathclyde, Glasgow G4 0NG, UK; ²School of Earth Sciences, University of Bristol, Bristol BS8 1RJ, UK; ³Institute of Solid State Physics, Technische Universität Berlin, Berlin D-10623, Germany; ⁴Tyndall National Institute, University College Cork, Cork T12 R5CP, Ireland and ⁵Ferdinand-Braun-Institut, Leibniz-Institut für Höchstfrequenztechnik, Berlin D-12489, Germany

Abstract

Wavelength-dispersive X-ray (WDX) spectroscopy was used to measure silicon atom concentrations in the range 35–100 ppm [corresponding to $(3\text{--}9) \times 10^{18} \text{ cm}^{-3}$] in doped $\text{Al}_x\text{Ga}_{1-x}\text{N}$ films using an electron probe microanalyser also equipped with a cathodoluminescence (CL) spectrometer. Doping with Si is the usual way to produce the *n*-type conducting layers that are critical in GaN- and $\text{Al}_x\text{Ga}_{1-x}\text{N}$ -based devices such as LEDs and laser diodes. Previously, we have shown excellent agreement for Mg dopant concentrations in *p*-GaN measured by WDX with values from the more widely used technique of secondary ion mass spectrometry (SIMS). However, a discrepancy between these methods has been reported when quantifying the *n*-type dopant, silicon. We identify the cause of discrepancy as inherent sample contamination and propose a way to correct this using a calibration relation. This new approach, using a method combining data derived from SIMS measurements on both GaN and $\text{Al}_x\text{Ga}_{1-x}\text{N}$ samples, provides the means to measure the Si content in these samples with account taken of variations in the ZAF corrections. This method presents a cost-effective and time-saving way to measure the Si doping and can also benefit from simultaneously measuring other signals, such as CL and electron channeling contrast imaging.

Key words: electron probe microanalysis, secondary ion mass spectrometry, semiconductor analysis, silicon doping, trace-element analysis

(Received 13 July 2020; revised 22 April 2021; accepted 16 May 2021)

Introduction

Wide band-gap semiconductors, such as $\text{Al}_x\text{Ga}_{1-x}\text{N}$ and GaN, are used in a wide range of technologically important optical and electrical devices, including high brightness LEDs, high electron mobility transistors (HEMTs) and laser diodes (Roccaforte et al., 2018; Tsao et al., 2018). Controlled doping of these alloys is crucial for control of the electronic properties of the epitaxial layers and hence optimal device performance. Si and Mg are typically employed as the *n*- and *p*-type dopants, respectively, in both $\text{Al}_x\text{Ga}_{1-x}\text{N}$ and GaN (Van de Walle et al., 1999).

Optoelectronic devices operating in the ultraviolet (UV) spectral range and those used for high power, high frequency electronic devices require wider band-gap materials, and $\text{Al}_x\text{Ga}_{1-x}\text{N}$ with increasing AlN content ($x \geq 0.5$) is often the material of choice (Amano et al., 2020). It is challenging to effectively dope $\text{Al}_x\text{Ga}_{1-x}\text{N}$, with Si and Mg at such high AlN contents because as the bandgap increases the ionization energies also increase. At the same time, a very high Si doping concentration is needed

to achieve low resistivity $\text{Al}_x\text{Ga}_{1-x}\text{N}$ layers (Mehnke et al., 2016; Foronda et al., 2020).

The procedure of quantitative measurement of Si concentration in semiconductor layers will enable the optimization of growth conditions in order to achieve high efficiency devices. In this paper, wavelength-dispersive X-ray (WDX) spectroscopy within an electron probe microanalyser (EPMA) was employed to measure donor levels. The WDX technique is routinely used for the quantification of major elements (concentration > 1,000 ppm) and minor elements (100–1,000 ppm), and during the last decade, it has been successfully used for trace-element analyses (below 100 ppm and down to 10 ppm) (Donovan et al., 2011). WDX analysis has several advantages over other analytical methods such as dynamic secondary ion mass spectrometry (D-SIMS), energy-dispersive X-ray spectroscopy (EDX), laser ablation inductively coupled plasma mass spectrometry (LA-ICP-MS), and micro particle-induced X-ray emission (μ -PIXE). These include high lateral spatial resolution (sub- μm), its nondestructive nature and that it does not usually require extensive standards due to the existence of well-developed matrix correction procedures. In addition, the EPMA allows acquisition of other analytical signals simultaneously with the high-resolution composition mapping, such as cathodoluminescence (CL; Martin et al., 2004; Lee et al., 2005; Edwards & Martin, 2011; Edwards et al., 2012),

*Authors for correspondence: Lucia Spasevski, E-mail: lucia.spasevski@strath.ac.uk; Robert W. Martin, E-mail: r.w.martin@strath.ac.uk

Cite this article: Spasevski L et al (2021) Quantification of Trace-Level Silicon Doping in $\text{Al}_x\text{Ga}_{1-x}\text{N}$ Films Using Wavelength-Dispersive X-Ray Microanalysis. *Microsc Microanal* 27, 696–704. doi:10.1017/S1431927621000568

electron beam-induced current (EBIC; Wallace et al., 2014), and electron channeling contrast imaging (ECCI) signals (Naresh-Kumar et al., 2020). Some limitations of the WDX technique are that depth resolution is a function of the electron accelerating voltage, which must be high enough to excite all the relevant X-ray lines, preferably with an overvoltage ratio of at least 2 to ensure accurate analysis, particularly when approaching detection limits. These limitations also introduce constraints on the minimum sample thickness (Newbury, 2002) and depth profiling, where SIMS performs strongly including for nitride semiconductor structures (Martin et al., 2006; Wei et al., 2014; Michałowski et al., 2019; Pickrell et al., 2019). Two of these works employed time-of-flight SIMS (TOF-SIMS) which has a number of advantages over D-SIMS, including dual-source depth profiling where the two ion beams have been optimized for their respective tasks, although work is needed to achieve the same detection limit for dopants (Klump et al., 2018).

The capability of the WDX technique for measuring dopants within semiconductor epilayers has been reported by Deatcher et al. (2006) and Kusch et al. (2017). The latter compared WDX data for Si concentration ranges 40–350 ppm (3×10^{18} – $2.8 \times 10^{19} \text{ cm}^{-3}$) in $\text{Al}_x\text{Ga}_{1-x}\text{N}$ with commercially performed D-SIMS on some of the samples in the study. Both measurement methods showed the same general trend: a linear increase in the Si concentration with increasing SiH_4/III (silane to group-III ratio), but the Si concentration measured by WDX was higher by a factor of approximately 2 compared with D-SIMS. The reason for the discrepancy between the different types of measurement was not clarified at the time (Kusch et al., 2017). However, the reports in Deatcher et al. (2006) and Robin et al. (2016) show that it is possible to use X-ray microanalysis to measure doping levels in semiconductor epilayers, with Robin et al. using EDX to address quantitation of dopants. The report of Deatcher et al. (2006) shows that Mg measurement in GaN gives very good agreement between WDX and D-SIMS. The question of why WDX measurement appears to over-estimate values for the Si doping is the subject of this investigation. Donovan et al. (2011) developed optimum measurement practices for WDX trace analysis which we will apply in the analysis of Si doping.

Over the years, many research groups have addressed the trace-element capabilities of the WDX technique. Some early examples include the analysis of Ge distribution in iron meteorites (Goldstein, 1967), transition elements in ferromagnesian silicate minerals (Merlet & Bodinier, 1990), trace elements in minerals (McKay & Seymour, 1982), and trace elements in glass (Fialin et al., 1999). More recent works focus on specific situations or on refinements of the technique and conditions for trace analysis, such as the works from Allaz et al. (2019), Batanova et al. (2018), Buse et al. (2018), Carpenter et al. (2002), Donovan et al. (2011, 2016), Fournelle (2007), von der Handt et al. (2016), Jercinovic et al. (2005, 2012), Reed (2000, 2002), Sato et al. (2007), and Zhang et al. (2016).

In this paper, we will consider how to measure Si, at dopant levels, in semiconductor epilayers such as GaN and $\text{Al}_x\text{Ga}_{1-x}\text{N}$ where inherent contamination of the sample surfaces with additional Si is suspected to be the cause of a discrepancy between the results from D-SIMS and WDX. Si incorporation is known to be a contaminant during the metal-organic chemical vapor deposition (MOCVD) growth of GaN and $\text{Al}_x\text{Ga}_{1-x}\text{N}$ (Koleske et al., 2002; Pickrell et al., 2019). Typical growth temperatures are in the region of 1,100°C, in order to promote the breakup of the ammonia molecules and adatom mobility on the growing

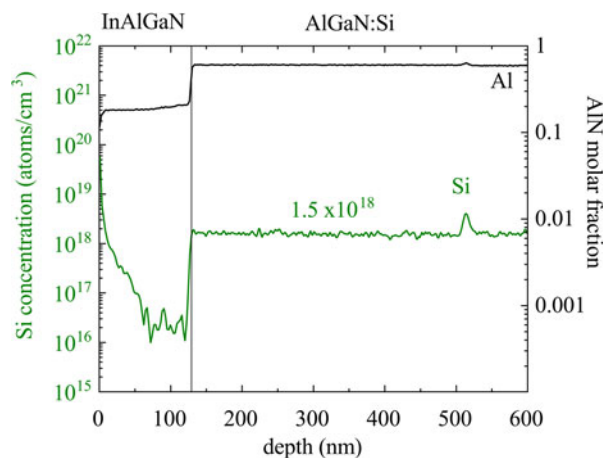


Fig. 1. SIMS profiles for Si and Al for a sample for which there was an interruption during the MOCVD growth. The sample consists of InAlGaN on top of a thick AlGaN:Si layer grown in two parts, with a change of reactors at a depth of approximately 500 nm.

surface, and it should be noted that the graphite susceptors used to heat and support the substrate wafer during growth are often coated with SiC to provide robustness. It typically takes about 30 min for the samples to cool down from the growth temperature and possible sources of Si contamination during that period include the reactor walls, precursors, substrates, or quartz liners (as molten Ga can etch the quartz to produce gallium oxide and free silicon). It is possible that there is a constant background source of Si within the reactor and the incorporation of Si has been shown to increase sharply when the ammonia flow drops (Koleske et al., 2002). After removing a sample from the growth chamber, silicate dust in the air and silicone oils are a likely source of Si contamination of the surfaces. SIMS data for samples where there has been a growth interruption to allow transfer between reactors reveal contamination with Si. This is illustrated in Figure 1 for an AlGaN:Si layer grown in two stages. The spike in the Si trace at a depth of approximately 500 nm shows a significant increase in its concentration at the interruption interface. Such a spike has also been observed in samples where there is no Si doping as well as ones where there was simply a pause in epitaxy, with no change in the reactor, to allow changes in growth parameters such as temperature and pressure. SIMS profiles from Pickrell et al. (2019) reveal significantly greater Si concentration in GaN due to air contamination when compared with growth interruptions with temperature ramps. In both cases, the oxygen trace remained at the detection limit.

Furthermore, a number of groups fabricating GaN-based nanowires have discussed Si-rich layers forming on the surface of nanowires grown with high silane flows and which impact the lateral-to-vertical growth rates (Tessarek et al., 2014; Ren et al., 2018). These layers are clearly visible in EDX maps obtained using transmission electron microscopy and although only a few nm thick contain high concentrations of Si.

Materials and Methods

The aim of this study was to explore the use of WDX in a commercial EPMA (JEOL JXA-8530F) to simultaneously measure the concentration of major (alloy) and minor (dopant) elements within semiconductor epilayers at specific points on the sample surface. We demonstrate a new approach to correct for the

Table 1. Reference GaN and Al_xGa_{1-x}N Samples for Which Independent Measurement of the Si Concentration Is Available.

Sample name	AlN at. %	Si net (Peak intensity-background intensity) (cps/ μ A)	WDX concentration ($\times 10^{18}$ cm ⁻³)	SIMS concentration ($\times 10^{18}$ cm ⁻³)	WDX concentration ($\times 10^{18}$ cm ⁻³) from the University of Bristol EPMA lab
TS4142 (GaN)	0	188 \pm 16	6.2 \pm 0.6 (coated)	0.743	10.0 \pm 2.0
			6.5 \pm 0.7 (uncoated)		
TS4137 (GaN)	0	208 \pm 19	6.3 \pm 0.4 (coated)	0.212	20.0 \pm 0.9
			10 \pm 2 (uncoated)		
TS5541 (“blank” Al _x Ga _{1-x} N), control sample	76 ^a	192 \pm 44	7.0 \pm 2.0	0 ^a	–
TS2039 (Al _x Ga _{1-x} N)	94 \pm 3 ^b	220 \pm 22	9.0 \pm 0.3	3.6 \pm 0.7	7.0 \pm 0.6
TS1860 (Al _x Ga _{1-x} N)	80 \pm 3 ^{bc}	306 \pm 27	9.0 \pm 0.4	4.1 \pm 0.8	10.0 \pm 2.0
				7.0 \pm 4.0	
EU2000894 (GaN)	0 ^c	857 \pm 44	40.0 \pm 3.0	12.0 \pm 0.6	–
				13	
TS5565 (Al _x Ga _{1-x} N)	57	634 \pm 5	21.4 \pm 0.5 (uncoated)	8.3	–
TS5587 (Al _x Ga _{1-x} N)	62	1,062 \pm 15	27.3 \pm 2.0 (uncoated)	13.4	–
TS5712 (Al _x Ga _{1-x} N)	79	506 \pm 10	14.8 \pm 0.5 (uncoated)	4.0	–
TS5770 (Al _x Ga _{1-x} N)	80	260 \pm 11	7.6 \pm 0.9 (uncoated)	1.4	–
TS5602 (Al _x Ga _{1-x} N)	60	1,700 \pm 36	37.1 \pm 3.7 (uncoated)	20.8	–

^aSample TS5541 has not been measured by SIMS, but it was grown undoped, so the SIMS concentration is assigned to be 0; AlN at.% as estimated from the growth conditions.

^bFrom Kusch et al. (2017).

^cSamples TS1860 and EU2000894 were measured by two of the three SIMS companies.

overestimation in measured Si donor concentration caused by inherent contamination of the sample surfaces with additional Si.

A range of Si-doped GaN and Al_xGa_{1-x}N samples, grown by MOCVD by different groups, were used to clarify the best way to measure Si. GaN:Si material (sample EU2000894) was provided by IQE Europe Ltd. A series of Al_xGa_{1-x}N samples with different crystal polarities and different AlN contents was provided by the Tyndall Institute. These Al_xGa_{1-x}N samples included polar-oriented [0001] (samples AP, BP, CP) and semipolar-oriented layers [112-2] (samples ASP, CSP). More details on the growth of the Al_xGa_{1-x}N:Si layers from the Tyndall Institute are given elsewhere (Li et al., 2013; Dinh et al., 2016a, 2016b; Pampili et al., 2018; Spasevski et al., 2021). Samples labeled TS are Al_xGa_{1-x}N layers with various AlN contents and crystal polarities grown at Technische Universität Berlin (Knauer et al., 2013; Kusch et al., 2014; Mehnke et al., 2016; Foronda et al., 2020). The “blank” Al_xGa_{1-x}N TS5541 was grown with no Si doping and quickly shipped in a sealed container filled with N₂ gas in order to minimize contamination and on receipt it was immediately placed under vacuum within the EPMA chamber. Information on the three sets of samples is given in Tables 1 and 2. Attempts were made to remove inherent surface contamination by oxygen plasma cleaning treatments. Traditionally, plasma cleaning is employed to remove hydrocarbon contamination (Donovan & Rowe, 2005). Apart from contamination, the samples can also suffer from oxidation. To investigate the effect of oxidation of the Si standard, cleaning with HF solution was employed.

D-SIMS data were provided by three different companies: RTG Mikroanalyse GmbH Berlin (Jörchel et al., 2016), Loughborough Surface Analysis Ltd. (using a CAMECA 7f), and Evans Analytical Group (EAG). All samples were analyzed in a depth profile mode, using areas typically 100 \times 100 μ m. RTG used ion-implanted AlGa_{1-x}N samples to produce absolute and relative sensitivity factors for Si in AlGa_{1-x}N, with further details given in Jörchel et al. (2016). The same approach was used for data from Loughborough. EAG used a proprietary method that calculates the change in sensitivity factors with respect to the AlN fraction in AlGa_{1-x}N.

WDX measurements were performed in the EPMA with the incident electron beam normal to the sample surface, and an acceleration voltage of 10 kV which is sufficient to efficiently excite the selected X-ray lines. Under these conditions, the electron interaction volume is kept within the first 500–800 nm of the Al_xGa_{1-x}N layer according to Monte Carlo simulations using CASINO software (Drouin et al., 2007) and dependent on the AlN molar content. In all samples, the interaction volume is contained within the top most Al_xGa_{1-x}N layer. The beam current was 40 nA for analysis of the major elements (Al, Ga, N) and increased to 400–500 nA for the minor elements. The beam was defocused to 10 or 20 μ m to improve sample averaging and avoid damaging the sample. The samples and standards were carbon coated to remove charging effects, with a thickness of approximately 15 nm [as determined by the interference-color method of Kerrick et al. (1973)]. This becomes increasingly important for AlN-rich Al_xGa_{1-x}N for which the conductivity decreases. Measurements were also performed on

Table 2. List of $\text{Al}_x\text{Ga}_{1-x}\text{N}$ Samples for Which Independent Constraint on the Composition Is Not Available, Measured AlN at.% Using WDX and Si K_α Intensity Values Together with the Calculated Si Concentration (Crystal Orientation [0001] AxP, Orientation [112] AxSP).

Sample name	WDX AlN at. %	WDX Si net (cps/ μA)	Calculated ZAF factor for the Si K_α in $\text{Al}_x\text{Ga}_{1-x}\text{N}$	Calculated Si concentration (10^{18} cm^{-3}) using the calibration method and calcZAF software	Calculated Si concentration (ppm) using the calibration method and calcZAF software
A1SP	56.6 \pm 0.6	175 \pm 16	1.283	3.1	31
A2SP	65.5 \pm 0.7	440 \pm 13	1.289	5.7	61
A3SP	61.2 \pm 0.7	469 \pm 54	1.286	6.2	65
A4SP	59.4 \pm 0.7	463 \pm 19	1.285	6.2	64
A5SP	59.6 \pm 0.7	374 \pm 10	1.285	5.2	54
A1P	63.0 \pm 0.7	218 \pm 33	1.287	3.4	36
A2P	71.7 \pm 0.8	253 \pm 22	1.294	3.5	40
A3P	68.8 \pm 0.7	320 \pm 6	1.292	4.3	47
A4P	62.7 \pm 0.7	534 \pm 9	1.287	6.8	72
A5P	69.3 \pm 0.7	743 \pm 9	1.292	8.6	96

two of the GaN:Si sample without coatings (and using uncoated standards) to confirm that the coating was not a source of Si.

According to best practice for trace analysis, the pulse height analysis (PHA) parameters (such as voltage window, baseline, electronic bias, and gain on the detector) were adjusted before measuring the Si K_α peak, using counter energy distributions of the peak on a pure Si standard with a beam current of 20 nA (Reed, 2002). Si has the tendency for a peak shift due to valence and coordination (Fournelle, 2006), but in our case, the shifts in the Si K_α peak position between pure Si standard and the unknown samples were insignificant. The differential mode was employed simply to exclude noise peaks and no higher-order interferences were observed in the region of the Si K_α peak (Geller & Herrington, 2002; Zhang et al., 2016).

In this paper, two methods were employed for checking the presence of Si dopants: qualitative and quantitative measurement. In the qualitative scan, the information on the element concentration is present in the height of the peak, extracted as peak maximum minus interpolated background. For the quantitative measurements, the EPMA's standard ZAF correction procedure was used in the usual way to determine the Si concentration and the results are included in Table 1. The quantitative procedure improves counting statistics due to the extended time spent acquiring peak and background X-rays, compared with the qualitative scan. The concentration of the major elements is quantified using the ratios of the background-corrected peak intensities for the sample to the corresponding ones obtained from AlN, GaN, and Si standards (k -ratios). Signals were acquired for 60 s on the peak positions and for 30 s on the background positions with a beam current of 20 nA. Ga L_α and Al K_α signals were recorded using a TAPH crystal (thallium acid phthalate, 100 mm Rowland circle), while for the N K_α signal, a synthetic layered LDE1L crystal (140 mm Rowland circle) was used. For quantification of the minor element, the Si K_α X-rays were recorded using a large TAP crystal (140 mm Rowland circle). The measured intensities are corrected for differences in composition between standard and specimen using the standard ZAF correction procedures in the JEOL EPMA software. The ZAF method consists of corrections for atomic number (Philibert-Tixier method), absorption (Philibert method), and fluorescent excitation (Reed method). The low silicon

concentrations necessitate a separate measurement routine to that for the major elements, due to different requirements for the counting statistics between the major and minor elements (Sato et al., 2007). Therefore, to improve counting statistics, longer measurement times and higher currents were employed: 400–500 nA, and 360 and 180 s counting times for the peak and background, respectively. The accelerating voltage and measurement positions were kept unchanged in order to ensure that the data for the silicon and major elements will refer to the same volumes within the sample. Unlike an EDX detector, WDX spectrometers record only one wavelength at a time so there is no risk of oversaturating the detector with major element counts when measuring silicon with high current. With the new measurement condition, the counting statistics were significantly improved for silicon and the counting error was reduced to 1–3% relative, with detection limit (DL) reduced to 1 ppm. Despite the smaller errors in the silicon signal, the final silicon concentration in the sample still resulted in higher concentrations [(0.6–4) $\times 10^{19} \text{ cm}^{-3}$ levels] than expected when compared with SIMS data available for the same samples.

In order to check the accuracy of measured results, an inter-laboratory study was conducted and some samples were also measured on the EPMA (JEOL JXA-8530F) at the University of Bristol.

Results and Discussion

In order to test the detection limit of approximately 10 ppm (1σ), which corresponds to concentrations of 10^{18} cm^{-3} of Si in GaN, we performed WDX measurements on two GaN: Si samples (TS4142 and TS4137) with low silicon contents that were also characterized by SIMS (Table 1), and on one “blank” $\text{Al}_x\text{Ga}_{1-x}\text{N}$ sample TS5541. Figure 2 shows long qualitative WDX scans (dwell time 12 s, 505 points, total time: 1 h 36 min), which were performed to check for the existence of the Si K_α peak. A Si peak is clearly visible above the background level in all of the above-mentioned samples (even in the “blank” sample, referred from now on as a control sample) and much greater than error/detection limit. We conclude that sample TS5541 is not actually blank and has accrued Si either during growth or in the time before measurement. From the qualitative scans, it is also possible

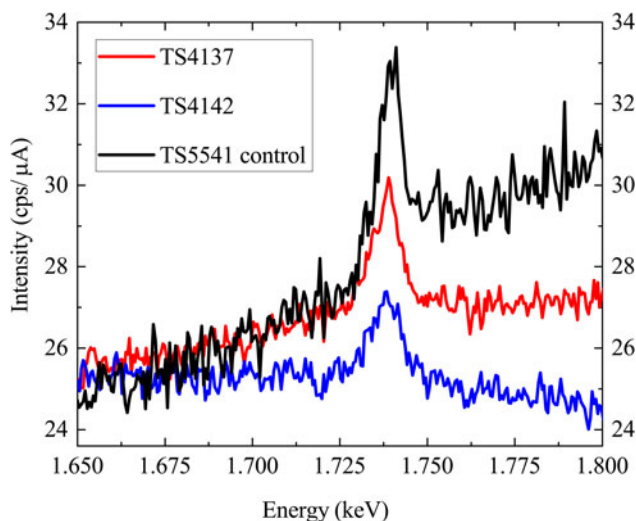


Fig. 2. Long qualitative scan (dwelt time 12 s) for the Si K_{α} peak from GaN:Si samples: TS4142 (blue), TS4137 (red), and $\text{Al}_x\text{Ga}_{1-x}\text{N}$ control sample TS5541 (black) using a TAPL crystal at 10 kV, 400 nA (100 nA for the control sample).

to conclude that there are no signs of any interference close to the Si K_{α} peak that could be a serious source of error in quantitative microanalysis and that the peak position is the same in the tested samples (Donovan et al., 1993). There are differences in the shape of the background for the samples shown in Figure 2, with the main difference being the high Al content in TS5541 which could be responsible for the increased background on the high-energy side for this sample.

Since the SIMS measurements (for the GaN samples) gave values below or close to the detection limit, the silicon doping should have been unmeasurable in these cases. However, the WDX data show clear Si X-ray peaks and high apparent Si content ($>6 \times 10^{18} \text{ cm}^{-3}$ compared with $<7 \times 10^{17} \text{ cm}^{-3}$ from the SIMS value in Table 1). Furthermore, the WDX analysis returned a similar value for Si concentration from the control sample. Measurements performed at the University of Bristol for GaN samples (TS4142 and TS4137, Table 1) gave similar Si concentrations ($\times 1.6$ and $\times 2$ higher, respectively). A different set of analytical conditions was used for the measurement, with a 400 nA current and $10 \mu\text{m}$ spot size. The above results appear to confirm that the samples are contaminated with Si in a way that would prevent convergence of the WDX and SIMS results by any simple adjustment of the analysis conditions. Attempts were, therefore, made to remove the contamination by cleaning treatments. *Ex situ* plasma cleaning did not result in any conclusive change when comparing Si content before and after cleaning (not shown).

Another possible reason for high Si values could be the existence of surface layers of native oxide formed on the standards. Oxidation of the standard will reduce the standard intensity due to the native oxygen layer and cause an overestimate of the concentration in the unknown (Merlet & Llovet, 2012). The silicon standard will form native layers of oxygen on the surface. Therefore, cleaning in HF solution was employed to remove the oxide layer from the Si standard. Qualitative scans around the Si peak were performed before and after cleaning (not shown), and Si K_{α} intensity data were acquired on the Si standard before and after the cleaning to check the difference (Table 3).

Table 3 shows that removal of the oxidation layer from the standard did not produce any significant changes (only 3–4%)

Table 3. Si K_{α} Intensities Acquired for Pure Si Standard, Before and After Removal of Native Oxide Layer.

TAPL crystal, 20 nA, 10 kV	Before cleaning (counts)	After cleaning (counts)	Percentage difference (%)
Uncoated	76,313	79,353	4
Coated	78,596	80,823	3

in the intensity of Si K_{α} peak. We can assume that the native oxygen layer was thinner than 10 nm (Carpenter, 2008).

Thus, as far as we can tell, cleaning treatments did not remove possible Si contamination and that oxidation of the sample or standard is not the reason for the large discrepancy between SIMS and WDX results. The data measured from two GaN:Si samples, with and without C-coating, confirm that the C-coat is not the source of extra Si.

After cleaning the Si standard, calibration data was acquired from it using a very low current of 1 nA in order to reduce the count difference between the standard and unknown trace element. This did not result in any difference in the measured concentration for the trace element when compared with calibration data acquired with 20 nA. Subsequently, all calibration data are acquired with a lower beam current of 20 nA compared with the 500 nA employed to measure Si in the unknowns, in order to avoid detector oversaturation. In doing this, we have relied on the current measurement system scaling linearly from 20 to 500 nA.

Due to the long measurement time and high currents used for the silicon analysis, the instrumental and sample stability need to be checked (Hughes et al., 2019). A sample will generally be stable during analysis with usual operating conditions (10–100 nA), but the high currents (hundreds of nA) required for trace-element analysis may cause it to degrade (Carpenter et al., 2002). It is necessary to assess if the samples are stable during measurement time due to potential charge build-up, heating or radiation damage. This was assessed by monitoring the count rate for Si K_{α} in one of the calibration samples at the same time as the absorbed current. Figure 3 shows that the silicon signal remains stable during the long counting times and there is only a very slight decrease of the absorbed current (0.3%). Since the measured absorbed current is not showing a significant drop or oscillations, it implies that the electrical properties of the coating are sufficient. The time scan was performed with a $10 \mu\text{m}$ defocused beam to simulate more extreme conditions, while the quantitative analysis sometimes used a beam diameter of $20 \mu\text{m}$ in order to minimize any absorbed current instability (Jercinovic & Williams, 2005).

The results of all the tests described so far lead us to propose that the best solution for using WDX for the accurate measurement of doping in $\text{Al}_x\text{Ga}_{1-x}\text{N}$ samples is to generate a calibration relation using samples also characterized by D-SIMS. The results listed in Table 1 are plotted in Figure 4 and show that the Si net intensity value (peak minus background) does not go below about 200 cps/ μA even for the samples with very low Si contents, which we attribute to surface contamination with Si (samples TS4142, TS4137, TS5541). These samples (marked by the gray circle) are thus considered not suitable for calibration and we propose a calibration relation for Si concentrations down to a lower limit defined by an Si net value of 200 cps/ μA . Prior to generating this line, the impact of the host material must be accounted for as these samples consist of $\text{Al}_x\text{Ga}_{1-x}\text{N}$ with different AlN% contents (Table 2).

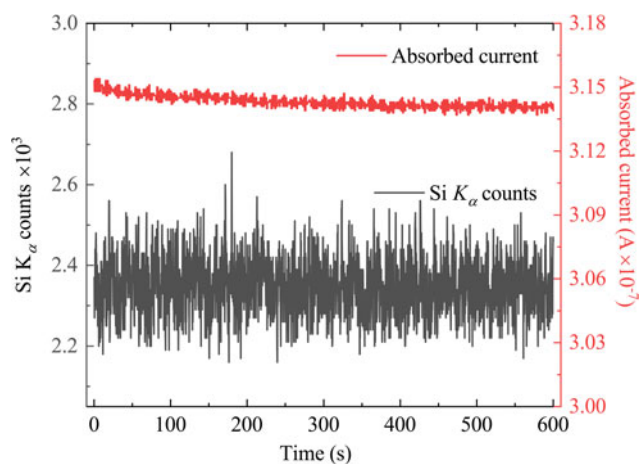


Fig. 3. Time scan for Si K_{α} in the GaN:Si calibration sample under “trace analysis” electron-beam operating conditions showing a constant Si K_{α} count rate and absorbed current as a function of time, showing only minor change in the absorbed current during long counting times.

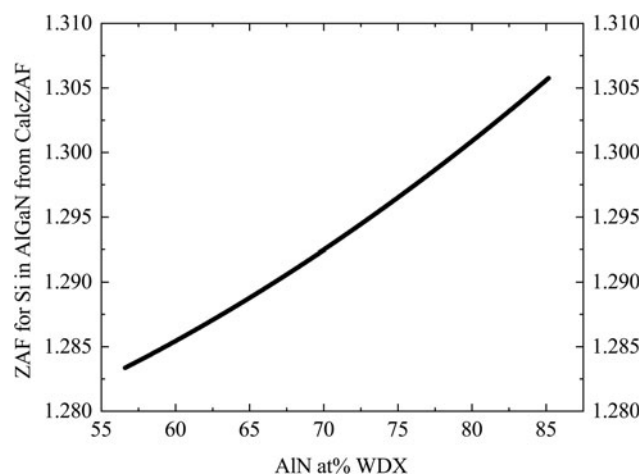


Fig. 5. Plot of the calculated matrix correction (ZAF correction) from elemental Si against AlN at.% as measured by WDX for each of the $\text{Al}_x\text{Ga}_{1-x}\text{N}$ samples.

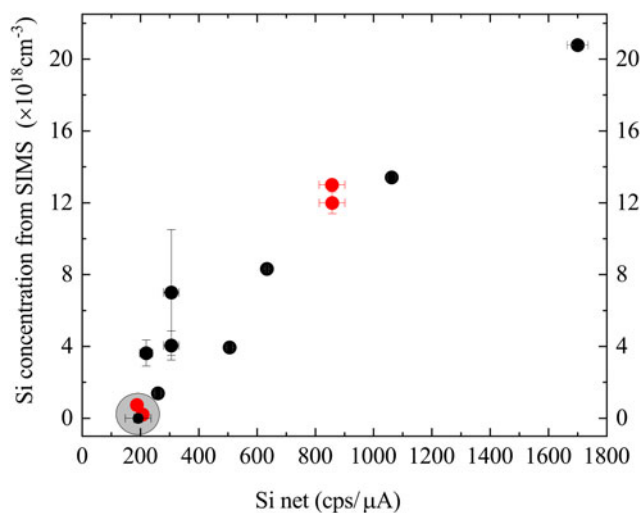


Fig. 4. Correlation between Si intensity measured by WDX and the concentration from SIMS data for GaN (red points) and $\text{Al}_x\text{Ga}_{1-x}\text{N}$ (black points) samples.

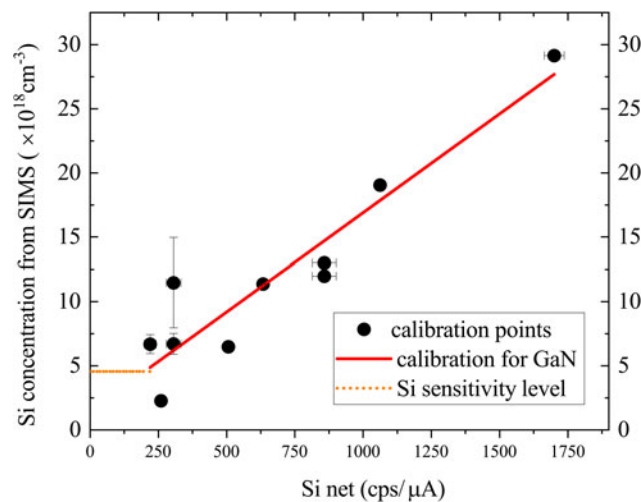


Fig. 6. Calibration relation with all the points representing Si intensity in GaN (For the $\text{Al}_x\text{Ga}_{1-x}\text{N}$ points, the Si concentration from D-SIMS is converted to its equivalent for GaN using CalcZAF software). The orange dotted line represents the Si sensitivity level for GaN.

The change in matrix correction (ZAF correction) for Si for different AlN contents was estimated using the stand-alone CalcZAF software (Donovan et al., 2019), as plotted in Figure 5. The different correction procedures available in CalcZAF software did not produce a noticeable difference in the correction factors.

The calculated ZAF parameters are then used to adjust all the D-SIMS calibration points to the effective value for a GaN host, as shown in Figure 6. This resulting calibration relation allows the Si content to be estimated in samples of all $\text{Al}_x\text{Ga}_{1-x}\text{N}$ compositions by measuring the Si intensity, then using the GaN calibration curve with the appropriate ZAF correction.

This process is illustrated using the series of $\text{Al}_x\text{Ga}_{1-x}\text{N}$ samples listed in Table 2. The measured intensity values, Si net (cps/ μA), are adjusted to the effective Si net values for GaN, using the ZAF correction procedure, and these are then converted to Si concentration using the calibration curve. The calculated Si concentrations in $\text{Al}_x\text{Ga}_{1-x}\text{N}$ are plotted in Figure 7, which also shows the calibration line for GaN for comparison. This method

enables the Si concentration in $\text{Al}_x\text{Ga}_{1-x}\text{N}$ samples of any composition to be estimated by measuring the Si intensity. For samples with Si net ≤ 200 cps/ μA (e.g. sample A1SP), the equivalent Si concentration is set to the sensitivity limit of 35 ppm, which corresponds to concentrations ranging from $2.4 \times 10^{18} \text{ cm}^{-3}$ for AlN or $4.6 \times 10^{18} \text{ cm}^{-3}$ for GaN, calculated from the calibration curve in Figure 6.

Figure 8 plots the calculated Si concentrations against the disilane to group III ratios ($\text{Si}_2\text{H}_6/\text{III}$ ratios) (Dinh et al., 2016a, 2016b; Pampili et al., 2018). In MOCVD growth, the group III atoms are introduced via metal precursors in the form of organic compounds such as trimethylgallium and trimethylaluminium, while ammonia is the nitrogen source. Doping can be obtained by introducing into the reactor dopant-containing gases, such as disilane (Si_2H_6) (Pampili & Parbrook, 2017). The measured Si concentrations for the semipolar ASP samples increase linearly with the $\text{Si}_2\text{H}_6/\text{III}$ ratio up to a saturation point of 2.3×10^{-4}

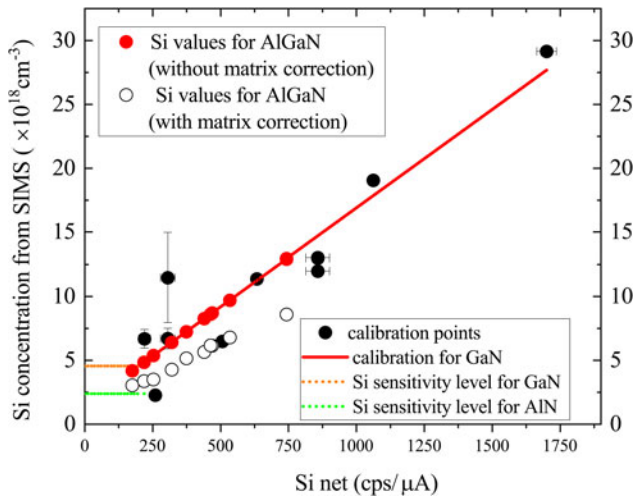


Fig. 7. Values for Si concentration in $\text{Al}_x\text{Ga}_{1-x}\text{N}$:Si layers plotted against the measured Si net signal. The line is the calculated calibration for GaN:Si and the points differ from this line according to the amount of AlN contained in the host material.

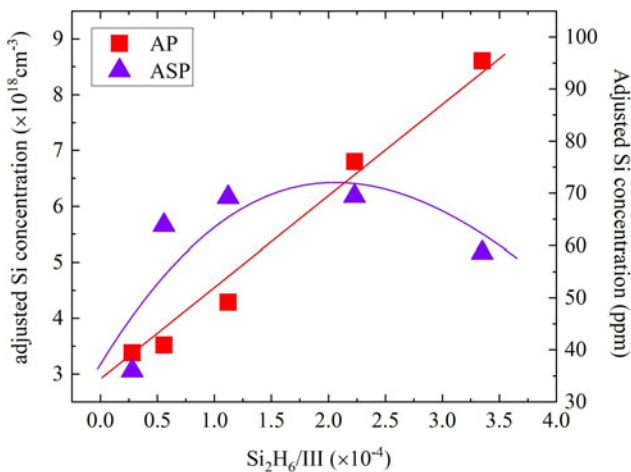


Fig. 8. Si concentration of the $\text{Al}_x\text{Ga}_{1-x}\text{N}$ -doped layer as a function of disilane to group III ratio, as evaluated by WDX. The solid lines provide guides to the eye.

$\text{Si}_2\text{H}_6/\text{III}$. The saturation point is consistent with a previous report from Dinh et al. (2016a), where the carrier concentration and mobility of semipolar layers were observed to reach a maximum at a similar $\text{Si}_2\text{H}_6/\text{III}$ ratio. The AP series exhibits an almost linear increase of Si with disilane flow rate.

Summary

The use of WDX spectroscopy for the measurement of silicon-doping levels in wide band-gap $\text{Al}_x\text{Ga}_{1-x}\text{N}$ layers is demonstrated in a commercially available EPMA instrument. A previously reported limitation with over-estimates of the Si contents was thoroughly investigated and was assigned to surface contamination. An analytical routine was introduced for measuring the trace Si levels, consisting of separate measurement of Si with high current and long counting times followed by calibration using D-SIMS measurements. By measuring silicon intensities and using a calibration curve fit method using the D-SIMS data along with calculated ZAF correction values, it was possible to determine doping levels of order $(3\text{--}10) \times 10^{18} \text{ cm}^{-3}$ in $\text{Al}_x\text{Ga}_{1-x}$

N layers with varying AlN contents and polarity. The highest values of Si incorporation were observed for polar samples (100 ppm), while saturation of Si incorporation was seen for semipolar samples at a high Si/III ratio. The advantages of the WDX approach include high lateral spatial resolution and the ability to determine the alloy composition of the major elements, such as Al, Ga, and N, at the same time as the doping levels. The standards used in WDX analysis are more accessible compared with ion-implanted standards required for the SIMS analysis. Apart from the quantitative abilities of the EPMA instrument, another major advantage in the examination of the semiconductor alloys is the correlation of WDX data with other microscopy techniques such as CL and ECCI as well as the high-resolution mapping capabilities.

Acknowledgments. The authors thank Dr. Trevor Martin from IQE Europe Ltd., for providing additional GaN:Si samples, and to Drs. Vitaly Zubialevich, Pietro Pampili, and Duc Dinh from Tyndall National Institute for providing additional AlGaIn:Si samples. We acknowledge Alison Chew of Loughborough Surface Analysis Ltd. for provision of D-SIMS measurement and discussion of the results. We thank Dr. Gunnar Kusch for useful discussion and advice. We thank Dr. Stacey Laing from the Department of Pure and Applied Chemistry, University of Strathclyde, for performing plasma cleaning of the samples. We would also like to show our gratitude to Mr. James Sweeney and Dr. Ian Watson from the Institute of Photonics, University of Strathclyde, for cleaning the samples with HF solution. This work was supported by the EPSRC project EP/N010914/1, “Nanoanalysis for Advanced Materials and Healthcare,” by the EU-FP7 programme “ALIGHT,” Science Foundation Ireland through SFI/10/IN.1/I2993 and Irish Photonic Integration Centre (SFI/12/RC/2276_2), and the European Space Agency. All data underpinning this publication are openly available from the University of Strathclyde KnowledgeBase at: <https://doi.org/10.15129/aa61c668-99ca-4802-9013-ff5f15409240>.

References

- Allaz JM, Razvan-Gabriel P, Reusser E & Martin L (2019). Electron microprobe analysis of minor and trace elements in beam sensitive materials: How far can we go? *Microsc Microanal* 25(S2), 2312–2313.
- Amano H, Collazo R, Santi CD, Einfeldt S, Funato M, Glaab J, Hagedorn S, Hirano A, Hirayama H, Ishii R, Kashima Y, Kawakami Y, Kirste R, Kneissl M, Martin R, Mehnke F, Meneghini M, Ougazzaden A, Parbrook PJ, Rajan S, Reddy P, Römer F, Rusch J, Sarkar B, Scholz F, Schowalter LJ, Shields P, Sitar Z, Sulmoni L, Wang T, Wernicke T, Weyers M, Witzigmann B, Wu Y-R, Wunderer T & Zhang Y (2020). The 2020 UV emitter roadmap. *J Phys D: Appl Phys* 53(50), 503001.
- Batanova VG, Sobolev AV & Magnin V (2018). Trace element analysis by EPMA in geosciences: Detection limit, precision and accuracy. *IOP Conf Ser: Mater Sci Eng* 304, 012001.
- Buse B, Wade J, Llovet X, Kearns S & Donovan JJ (2018). Secondary fluorescence in WDS: The role of spectrometer positioning. *Microsc Microanal* 24(6), 604–611.
- Carpenter P, Counce D, Kluk E & Nabelek C (2002). Characterization of cornering EPMA standard glasses 95IRV, 95IRW, and 95IRX. *J Res Natl Inst Stand Technol* 107(6), 703–718.
- Carpenter PK (2008). EPMA standards: The good, the bad, and the ugly. *Microsc Microanal* 14(S2), 530–531.
- Deatcher C, Bejtka K, Martin R, Romani S, Kheyrandish H, Smith L, Rushworth S, Liu C, Cheong M & Watson I (2006). Wavelength-dispersive X-ray microanalysis as a novel method for studying magnesium doping in gallium nitride epitaxial films. *Semicond Sci Technol* 21, 1287–1295.
- Dinh DV, Alam SN & Parbrook PJ (2016a). Effect of V/III ratio on the growth of ([112̄]) AlGaIn by metalorganic vapour phase epitaxy. *J Cryst Growth* 435, 12–18.
- Dinh DV, Pampili P & Parbrook PJ (2016b). Silicon doping of semipolar ([112̄]) $\text{Al}_x\text{Ga}_{1-x}\text{N}$ ($0.50 \leq x \leq 0.55$). *J Cryst Growth* 451, 181–187.

- Donovan J, Pinard P & Demers H (2019). High speed matrix corrections for quantitative X-ray microanalysis based on Monte Carlo simulated K-ratio intensities. *Microsc Microanal* 25(3), 735–742.
- Donovan J & Rowe M (2005). Techniques for improving quantitative analysis of mineral glasses. *Geochim Cosmochim Acta* 69(Suppl 10), 589.
- Donovan JJ, Lowers HA & Rusk BG (2011). Improved electron probe microanalysis of trace elements in quartz. *Am Mineral* 96(2–3), 274–282.
- Donovan JJ, Singer JW & Armstrong JT (2016). A new EPMA method for fast trace element analysis in simple matrices. *Am Mineral* 101(8), 1839–1853.
- Donovan JJ, Snyder DA & Rivers ML (1993). An improved interference correction for trace element analysis. *Microbeam Anal* 2, 23–28.
- Drouin D, Couture AR, Dany J, Tastet X, Aimez V & Gauvin R (2007). CASINO v2.42—A fast and easy-to-use modeling tool for scanning electron microscopy and microanalysis users. *Scanning* 29(3), 92–101.
- Edwards PR, Jagadamma LK, Bruckbauer J, Liu C, Shields P, Allsopp D, Wang T & Martin RW (2012). High-resolution cathodoluminescence hyperspectral imaging of nitride nanostructures. *Microsc Microanal* 18(6), 1212–1219.
- Edwards PR & Martin RW (2011). Cathodoluminescence nanocharacterization of semiconductors. *Semicond Sci Technol* 26(6), 064005.
- Fialin M, Remy H, Richard C & Wagner C (1999). Trace element analysis with the electron microprobe: New data and perspectives. *Am Mineral* 84(1–2), 70–77.
- Foronda HM, Hunter DA, Pietsch M, Sulmoni L, Muhin A, Graupeter S, Susilo N, Schilling M, Enslin J, Irmischer K, Martin RW, Wernicke T & Kneissl M (2020). Electrical properties of (11–22) Si:AlGaN layers at high Al contents grown by metal-organic vapor phase epitaxy. *Appl Phys Lett* 117(22), 221101.
- Fournelle J (2006). Silicate peak shifts, spectrometer peaking issues and standard/specimen size discrepancies in EPMA: 3 Bumps in the road to the goal of 1% accuracy. In *AGU Spring Meeting Abstracts*.
- Fournelle J (2007). Problems in trace element EPMA: Modeling secondary fluorescence with PENEPMA. In *AGU Fall Meeting Abstracts*, pp. V51A-0329.
- Geller JD & Herrington C (2002). High count rate electron probe microanalysis. *J Res Natl Inst Stand Technol* 107(6), 503–508.
- Goldstein JI (1967). Distribution of germanium in the metallic phases of some iron meteorites. *J Geophys Res* (1896–1977) 72(18), 4689–4696.
- Hughes EC, Buse B, Kearns SL, Blundy JD, Kilgour G & Mader HM (2019). Low analytical totals in EPMA of hydrous silicate glass due to sub-surface charging: Obtaining accurate volatiles by difference. *Chem Geol* 505, 48–56.
- Jercinovic M, Williams M, Allaz J & Donovan J (2012). Trace analysis in EPMA. *IOP Conf Ser: Mat Sci Eng* 32.
- Jercinovic MJ & Williams ML (2005). Analytical perils (and progress) in electron microprobe trace element analysis applied to geochronology: Background acquisition, interferences, and beam irradiation effects. *Am Mineral* 90(4), 526–546.
- Jercinovic MJ & Williams ML (2005). Analytical perils (and progress) in electron microprobe trace element analysis applied to geochronology: Background acquisition, interferences, and beam irradiation effects. *Am Mineral* 90(4), 526–546.
- Jörchel P, Helm P, Brunner F, Thies A, Krüger O & Weyers M (2016). Quantification of matrix and impurity elements in $\text{Al}_x\text{Ga}_{1-x}\text{N}$ compounds by secondary ion mass spectrometry. *J Vac Sci Technol B* 34(3), 03H128.
- Kerrick D, Eminhizer L & Villaume J (1973). The role of carbon film thickness in electron microprobe analysis. *Am Mineral* 58, 920–925.
- Klump A, Zhou C, Stevie FA, Collazo R & Sitar Z (2018). Improvement in detection limit for time-of-flight SIMS analysis of dopants in GaN structures. *J Vac Sci Technol B* 36(3), 03F102.
- Knauer A, Kueller V, Zeimer U, Weyers M, Reich C & Kneissl M (2013). Algan layer structures for deep UV emitters on laterally overgrown AlN/sapphire templates. *Phys Status Solidi (A)* 210(3), 451–454.
- Koleske DD, Wickenden AE, Henry RL & Twigg ME (2002). Influence of MOVPE growth conditions on carbon and silicon concentrations in GaN. *J Cryst Growth* 242(1), 55–69.
- Kusch G, Li H, Edwards PR, Bruckbauer J, Sadler TC, Parbrook PJ & Martin RW (2014). Influence of substrate miscut angle on surface morphology and luminescence properties of AlGaN. *Appl Phys Lett* 104(9), 092114.
- Kusch G, Mehnke F, Enslin J, Edwards PR, Wernicke T, Kneissl M & Martin RW (2017). Analysis of doping concentration and composition in wide bandgap AlGaN:Si by wavelength dispersive X-ray spectroscopy. *Semicond Sci Technol* 32(3), 7.
- Lee MR, Martin RW, Trager-Cowan C & Edwards PR (2005). Imaging of cathodoluminescence zoning in calcite by scanning electron microscopy and hyperspectral mapping. *J Sediment Res* 75(2), 313–322.
- Li H, Sadler TC & Parbrook PJ (2013). AlN heteroepitaxy on sapphire by metal-organic vapour phase epitaxy using low temperature nucleation layers. *J Cryst Growth* 383, 72–78.
- Martin RW, Edwards PR, O'Donnell KP, Dawson MD, Jeon C-W, Liu C, Rice GR & Watson IM (2004). Cathodoluminescence spectral mapping of III-nitride structures. *Phys Status Solidi (A)* 201(4), 665–672.
- Martin RW, Rading D, Kersting R, Tallarek E, Nogales E, Amabile D, Wang K, Katchkanov V, Trager-Cowan C, O'Donnell KP, Watson IM, Matias V, Vantomme A, Lorenz K & Alves E (2006). Depth profiling of ion-implanted AlInN using time-of-flight secondary ion mass spectrometry and cathodoluminescence. *Phys Status Solidi C* 3(6), 1927–1930.
- McKay G & Seymour R (1982). Electron microprobe analysis of trace elements in minerals at 10 PPM concentrations. *Proceedings, Annual Conference - Microbeam Analysis Society*.
- Mehnke F, Trinh XT, Pingel H, Wernicke T, Janzén E, Son NT & Kneissl M (2016). Electronic properties of Si-doped $\text{Al}_x\text{Ga}_{1-x}\text{N}$ with aluminum mole fractions above 80%. *J Appl Phys* 120(14), 145702.
- Merlet C & Bodinier J-L (1990). Electron microprobe determination of minor and trace transition elements in silicate minerals: A method and its application to mineral zoning in the peridotite nodule PHN 1611. *Chem Geol* 83(1), 55–69.
- Merlet C & Llovet X (2012). Uncertainty and capability of quantitative EPMA at low voltage – A review. *IOP Conf Ser: Mater Sci Eng* 32, 012016.
- Michałowski PP, Zlotnik S & Rudziński M (2019). Three dimensional localization of unintentional oxygen impurities in gallium nitride. *Chem Commun* 55(77), 11539–11542.
- Naresh-Kumar G, Alasmari A, Kusch G, Edwards PR, Martin RW, Mingard KP & Trager-Cowan C (2020). Metrology of crystal defects through intensity variations in secondary electrons from the diffraction of primary electrons in a scanning electron microscope. *Ultramicroscopy* 213, 112977.
- Newbury DE (2002). Barriers to quantitative electron microanalysis for low voltage electron microscopy. *J Res Natl Inst Stand Technol* 107(6), 605–619.
- Pampili P, Dinh DV, Zubialevich VZ & Parbrook PJ (2018). Significant contribution from impurity-band transport to the room temperature conductivity of silicon-doped AlGaN. *J Phys D: Appl Phys* 51(6), 06LT01.
- Pampili P & Parbrook PJ (2017). Doping of III-nitride materials. *Mater Sci Semicond Process* 62, 180–191.
- Pickrell GW, Armstrong AM, Allerman AA, Crawford MH, Cross KC, Glaser CE & Abate VM (2019). Regrown vertical GaN p–n diodes with low reverse leakage current. *J Electron Mater* 48(5), 3311–3316.
- Reed SJB (2000). Quantitative trace analysis by wavelength-dispersive EPMA. *Microchim Acta* 132(2), 145–151.
- Reed SJB (2002). Optimization of wavelength dispersive X-ray spectrometry analysis conditions. *J Res Natl Inst Stand Technol* 107(6), 497–502.
- Ren CX, Tang F, Oliver RA & Zhu T (2018). Nanoscopic insights into the effect of silicon on core-shell InGaN/GaN nanorods: Luminescence, composition, and structure. *J Appl Phys* 123(4), 045103.
- Robin E, Mollard N, Guillois K, Pauc N, Gentile P, Fang Z, Daudin B, Amichi L, Jouneau P, Bougerol C, Delalande M & Bavencove A (2016). Quantification of dopants in nanomaterial by SEM/EDS. *European Microscopy Congress 2016: Proceedings*.
- Roccaforte F, Fiorenza P, Greco G, Lo Nigro R, Giannazzo F, Iucolano F & Saggio M (2018). Emerging trends in wide band gap semiconductors (SiC and GaN) technology for power devices. *Microelectron Eng* 187–188, 66–77.
- Sato A, Mori N, Takakura M & Notoya S (2007). Examination of analytical conditions for trace elements based on the detection limit of EPMA (WDS). *JEOL News* 42E (No.1).
- Spasevski L, Kusch G, Pampili P, Zubialevich VZ, Dinh DV, Bruckbauer J, Edwards PR, Parbrook PJ & Martin RW (2021). A systematic comparison of polar and semipolar Si-doped AlGaN alloys with high AlN content. *J Phys D: Appl Phys* 54(3), 035302.

- Tessarek C, Heilmann M, Butzen E, Haab A, Hardtdegen H, Dieker C, Spiecker E & Christiansen S (2014). The role of Si during the growth of GaN micro- and nanorods. *Cryst Growth Des* **14**(3), 1486–1492.
- Tsao JY, Chowdhury S, Hollis MA, Jena D, Johnson NM, Jones KA, Kaplar RJ, Rajan S, Van de Walle CG, Bellotti E, Chua CL, Collazo R, Coltrin ME, Cooper JA, Evans KR, Graham S, Grotjohn TA, Heller ER, Higashiwaki M, Islam MS, Juodawlkis PW, Khan MA, Koehler AD, Leach JH, Mishra UK, Nemanich RJ, Pilawa-Podgurski RCN, Shealy JB, Sitar Z, Tadjer MJ, Witulski AF, Wraback M & Simmons JA (2018). Ultrawide-bandgap semiconductors: Research opportunities and challenges. *Adv Electron Mater* **4**(1), 1600501.
- Van de Walle CG, Stampfl C, Neugebauer J, McCluskey MD & Johnson NM (1999). Doping of AlGaIn alloys. *MRS Internet J Nitride Semicond Res* **4**(S1), 890–901.
- von der Handt A, Allaz J & Neill OK (2016). Microanalytical standards, reference and research materials: Continuing the effort toward breaking the accuracy barrier. *Microsc Microanal* **22**(S3), 424–425.
- Wallace MJ, Edwards PR, Kappers MJ, Hopkins MA, Oehler F, Sivaraya S, Allsopp DWE, Oliver RA, Humphreys CJ & Martin RW (2014). Bias dependence and correlation of the cathodoluminescence and electron beam induced current from an InGaIn/GaN light emitting diode. *J Appl Phys* **116**(3), 033105.
- Wei X, Zhao L, Wang J, Zeng Y & Li J (2014). Characterization of nitride-based LED materials and devices using TOF-SIMS. *Surf Interface Anal* **46**(S1), 299–302.
- Zhang C, Koepke J, Wang L-X, Wolff P, Wilke S, Stechern A, Almeev R & Holtz F (2016). A practical method for accurate measurement of trace level fluorine in Mg- and Fe-bearing mineral and glass using electron probe microanalysis. *Geostand Geoanal Res* **40**, 351–363.